Experimental investigation of mixing and axial dispersion in Taylor–Couette flow patterns

Marouan Nemri · Sébastien Cazin ·
Sophie Charton · Eric Climent

Abstract The flow and mixing in a Taylor–Couette device have been characterized by means of simultaneous particle image velocimetry and planar laser-induced fluorescence (PLIF) measurements. Concentration of a passive tracer measurements was used to investigate mixing efficiency for different flow patterns (from steady Taylor vortex flow to modulated wavy vortex flow, MWVF). Taylor–Couette flow is known to evolve toward turbulence through a sequence of flow instabilities. Macroscopic quantities, such as axial dispersion and mixing index, are extremely sensitive to internal flow structures. PLIF measurements show clear evidences of different transport mechanisms including intravortex mixing and tracer fluxes through neighboring vortices. Under WVF and MWVF regimes, intravortex mixing is controlled by chaotic advection, due to the 3D nature of the flow, while intervortex transport occurs due to the presence of waves between neighboring vortices. The combination of these two mechanisms results in enhanced axial dispersion. We show that hysteresis may occur between consecutive regimes depending on flow history, and this may have a significant effect on mixing for a given Reynolds number.

M. Nemri · S. Charton
CEA, DEN, DTEC, SGCS, 30207 Bagnols-sur-Cèze, France
e-mail: marouan.nemri@cea.fr

S. Charton
e-mail: sophie.charton@cea.fr

S. Cazin · E. Climent (✉)
Institut de Mécanique des Fluides de Toulouse (IMFT), CNRS,
Université de Toulouse, Allée Camille Soula, 31400 Toulouse,
France
e-mail: eric.climent@imft.fr

S. Cazin
e-mail: sebastien.cazin@imft.fr

List of symbols

Subscripts

c	Critical
i	Inner cylinder
e	Outer cylinder
r	Radial direction
θ	Azimuthal direction
x	Axial direction
$r-x$	Meridional plane
0	Initial condition

Variables

A	Area of pixels with value 1 $(-)$
C	Concentration $(-)$
$\overline{C}$	Mean concentration $(-)$
C_0	Injection concentration (g L^{-1})
C_f	Final concentration $(-)$
D_x	Dispersion coefficient (m^2 s^{-1})
da	Instantaneous area (m^2)
dA	Reference area (m^2)
e	Annular gap width (m)
f	Frequency (s^{-1})
f_{WVF}	Traveling wave frequency (s^{-1})
F	Spectral density of the gray level $(-)$
I	Intensity of segregation $(-)$
I_{rx}	Intensity of segregation in $(-)$ the meridional plane $(r-x)$
I_θ	Intensity of segregation in $(-)$ the azimuthal direction (θ)
I_v	Intensity of segregation $(-)$ between adjacent vortices
L	Column height (m)

m	Azimuthal wave number (−)
m_{inflow}	Azimuthal wave number in inflow zone (−)
$m_{outflow}$	Azimuthal wave number in outflow zone
n_D	Refraction index (−)
R	Radius (m)
Re	Reynolds number (−)
s	Area stretch (−)
S_a	Rate of stretching (s^{-1})
s_i	Vortex size (m^2)
S	Taylor-cell size (m^2)
t	Time (s)
t_{acc}	Acceleration time (s)
T_c	Inner cylinder rotational period (s)
T_d	Vortex center rotational period (s)
U	Velocity (m s^{-1})
V_ϕ	Phase velocity (rad s^{-1})
λ	Wavelength (m)
λ_x	Axial wavelength (m)
σ_c	Standard deviation of concentration (−)
σ_0	Mean max deviation (−)
η	Radius ratio (−)
μ	Dynamic viscosity (Pa s)
v	Kinematic viscosity (m^2 s^{-1})
ρ	Density (kg m^{-3})
Γ	Column aspect ratio (−)
Ω	Inner cylinder rotational speed (s^{-1})
Φ	Phase shift (−)

Abbreviations

RTD	Residence time distribution
PIV	Particle image velocimetry
PLIF	Planar laser-induced fluorescence
TVF	Taylor vortex flow
WVF	Wavy vortex flow
MWVF	Modulated wavy vortex flow
TTVF	Turbulent Taylor vortex flow
WIB	Wavy inflow boundary
WOB	Wavy outflow boundary

1 Introduction

Annular centrifugal contactors based on Taylor–Couette flow geometry have a great potential in chemistry, hydro-metallurgy and, since the prior works of Davis and Weber (1960), in the nuclear industry where they are particularly suitable for small-scale studies of solvent extraction processes. Since the pioneering work of Taylor (1923), Taylor–Couette flow has been extensively studied due to its nonlinear dynamics. It is an academic flow known to evolve toward turbulence through a sequence of successive hydrodynamic instabilities as the inner cylinder rotation rate increases. Beyond a critical speed of the rotating cylinder, pure azimuthal Couette flow results in the formation of toroidal vortices, called Taylor vortex flow (TVF). This critical condition is characterized by the Taylor number or equivalently by the Reynolds number (Re_c) based on the gap width e, the inner cylinder linear velocity ΩR_i and the fluid viscosity v. The Reynolds number is defined as:

$$Re = \frac{\Omega R_i e}{v} \tag{1}$$

At higher Reynolds numbers, a secondary instability causes the flow to become time dependent due to the appearance of an azimuthal wave (deformation of the vortices). This flow state, known as Wavy Vortex Flow (WVF), is characterized by an axial wavelength λ_x and an azimuthal wavenumber noted m. As Re further increases, the wavy flow becomes increasingly modulated by additional frequencies (MWVF) and eventually becomes turbulent (TTVF).

These flow instabilities have been the topic of many studies (Coles 1965; Fenstermacher et al. 1979; Andereck et al. 1985). Such flow patterns provide high values of heat and mass transfer coefficients, which explains why some important industrial operations, such as emulsion polymerization (Kataoka et al. 1995), heterogeneous catalytic reactions (Legrand and Coeuret 1986), bioreactor applications (Haut et al. 2003; Hill et al. 2006; Dusting and Balabani 2009) and liquid–liquid extraction (Davis and Weber 1960), can take advantage of Taylor–Couette device.

Mass transport in Taylor–Couette flow has been the subject of numerous experimental and numerical studies (Campero and Vigil 1997; Desmet et al. 1996a, b; Kataoka et al. 1975; Tam and Swinney 1987; Rudman 1998). Two main mechanisms are responsible for mixing: the intra-vortex mixing related to the velocity field within each vortex and the intervortex mixing related to the characteristics and topology of the flow connecting cellular patterns. Intravortex mixing consists in both circumferential mixing and meridional mixing. For TVF flow (Kataoka et al. 1975, 1977; Kataoka and Takigawa 1981), highlighted the existence of a weak intercell exchange which justify the assumption of considering each vortex as an independent cell. In order to model axial dispersion, most studies have used either the one-dimensional diffusion model or the multi-stirred tanks in series model (Kataoka et al. 1975; Tam and Swinney 1987; Moore and Cooney 1995). Later, Legrand and Coeuret (1986) have discussed the absence of intervortex transport which was contradicted by several authors (see for instance Pudijioni et al. 1992). As the rotation speed of the inner cylinder increases, the occurrence of wavy motion enhances intravortex mixing noticeably (Desmet et al. 1996a, b) as well as the

intervortex mixing (Akonur and Lueptow 2002). The wavy perturbation breaks the stream surface separating neighboring vortices which influence the axial dispersion. Desmet et al. (1996a) combined plug flow and mixing tank models into a single two zone model. In their model, the outer zone stands for the well-mixed fluid near boundaries and the inner zone corresponds to the vortex core. More recently, Campero and Vigil (1997) used the same approach as Desmet et al. (1996b) and proposed a 3-parameter model which takes into account non-ideal mixing in the inner region.

In the present study, mixing in Taylor–Couette flow patterns is investigated. We focus on the mixing mechanisms controlling the axial dispersion in wavy regimes. A global dispersion coefficient D_x is generally used to represent the mixing phenomena. Both numerical (Rudman 1998; Nemri et al. 2012) and experimental (Nemri et al. 2012) studies have revealed a significant effect of the flow state on the mixing properties. Indeed, in the wavy flow regimes (WVF and MWVF) where a multiplicity of wavy states can be achieved, D_x may vary significantly for the same Reynolds number. Our objective was to investigate the relation between the physics of the flow and axial mixing, using simultaneous PIV–PLIF measurements. We intended to quantify the respective role of intravortex and intervortex mixing on axial dispersion in both TVF and WVF regimes. The influence of the flow bifurcations as well as the multiplicity of wave states is also studied in order to understand the non-monotonic behavior of the axial dispersion coefficient observed in our previous study (Nemri et al. 2012).

2 Methodology

2.1 Description of the apparatus

The experimental device consists in two concentric cylinders with the inner one rotating and the outer cylinder fixed. A prototype, with gap width, $e = 11$ mm, was specially designed for specific optical investigations (PIV, PLIF). The geometry is characterized by the radius ratio η and the aspect ratio Γ (see Table 1). The main features of the experimental device are shown in Fig. 1.

The inner cylinder is driven by a reduction motor guided by a speed regulator system, with an accuracy of 0.008 rpm. A ramp generator controls the rotor acceleration during transient evolution to the desired Reynolds number. Indeed, for the same Reynolds number, Re, using different acceleration ramps provides various flow states (Dutcher and Muller 2009). Therefore, a given wave regime is selected by following one of the prescribed start-up protocols.

Table 1 Apparatus geometry and operating conditions

Parameters	Dimensions
Inner cylinder radius (R_i)	24 mm
Outer cylinder radius (R_e)	35 mm
Gap width ($e = R_e - R_i$)	11 mm
Radius ratio ($\eta = R_i/R_e$)	0.687
Length (L)	640 mm
Aspect ratio ($\Gamma = L/e$)	58
Inner cylinder rotation speed (Ω)	4–1,000 rpm

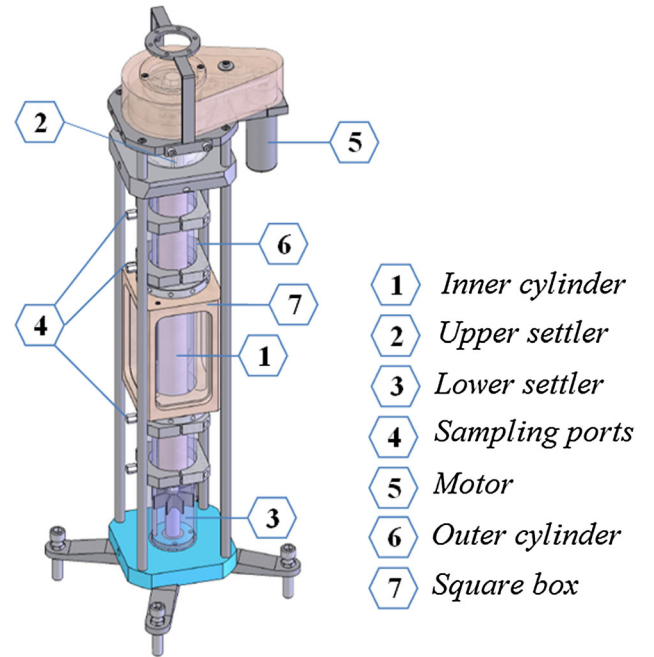|	
1	Inner cylinder
2	Upper settler
3	Lower settler
4	Sampling ports
5	Motor
6	Outer cylinder
7	Square box

Fig. 1 Schematic presentation of the apparatus

- An impulsive start from rest to the target rotation speed.
- A gradual acceleration from rest to the desired rotation speed at a constant rate during 300 s.
- A gradual deceleration from a specified rotation speed (Re_0) in turbulent regime to the desired rotation speed at a constant rate during 5 s.

This procedure ensures reproducibility of our measurements. For each case, the flow pattern was visualized in an aqueous solution seeded with Kalliroscope AQ-1000 flakes. These particles consist in small light-reflecting slabs which align themselves along streamlines. Using high-speed camera, the successive transitions can been identified (Fig. 2a, b). In order to fully characterize the different wavy regimes, a spectral analysis of the data was performed to determine the wave state (axial and azimuthal wave numbers). The different cases studied in this paper are summarized in Table 2. A visualization of two different wave states is shown in Fig. 2 with their respective power spectra.

Fig. 2 Multiplicity of wave states for $Re = 1,082$: **a** visualization of the $m = 5$ wave state ($\lambda_x = 3.40e$), **b** visualization of the $m = 3$ wave state ($\lambda_x = 3.47e$), **c** and **d** power spectra of the scattered light intensity for the two wave states corresponding, respectively, to (**a**) and (**b**), measured at the inflow boundary. F is the spectral density of the *gray* level
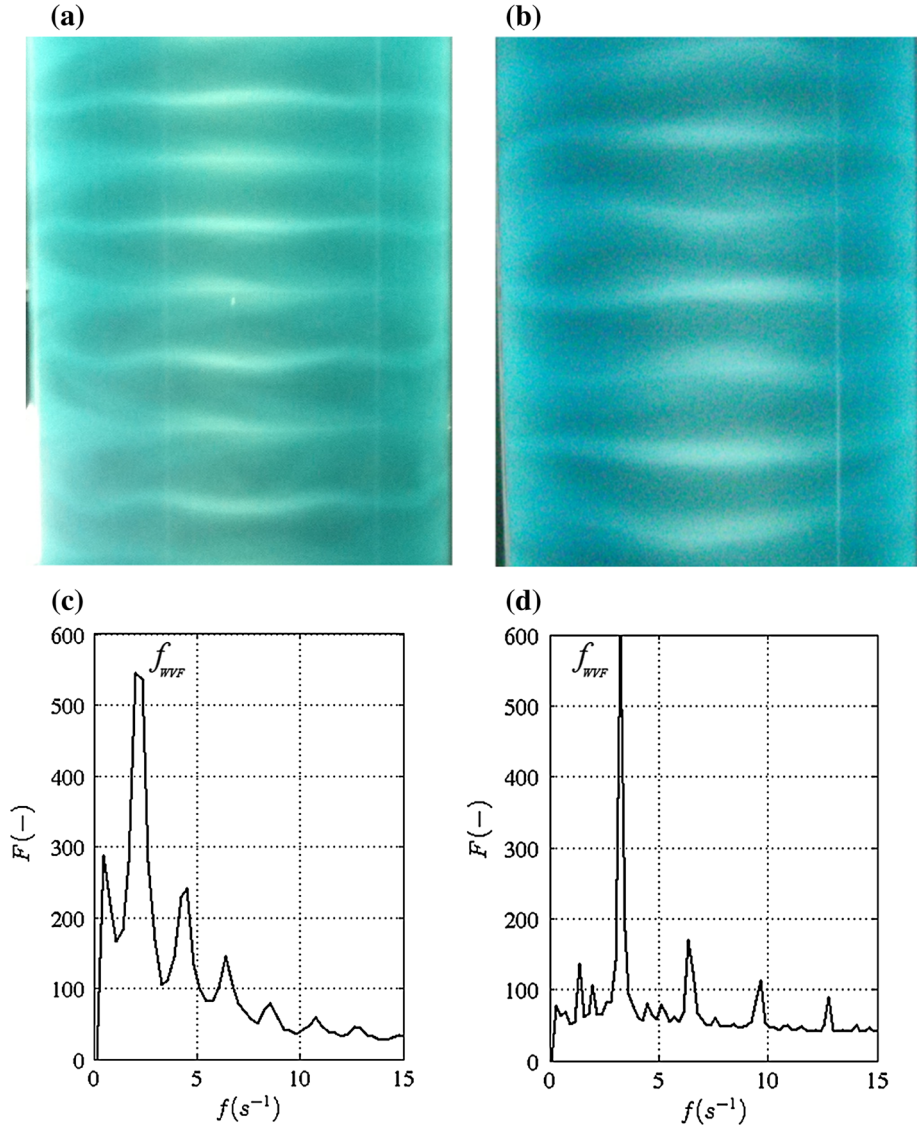

Table 2 Characteristics of the studied cases (Re, λ_x, m)

Re	Re_0	t_{acc}	λ_x	m_{inflow}	$m_{outflow}$	T_c (s)
382	0	1 s	2.05e	TVF	TVF	6
795	6,000	5 s	2.31e	4	No wave	1.2
795	0	1 s	2.11e	2	No wave	1.2
1,082	0	1 s	2.40e	4	1	0.9
1,082	0	300 s	2.47e	3	3	0.9
1,082	6,000	5 s	2.35e	5	1	0.9

t_{acc} is the duration of the acceleration ramp-measurements, Re_0 is the Reynolds number which corresponds to initial rotation rate used for start-up protocols, m_{inflow} is the azimuthal wave number in inflow zone and $m_{outflow}$ is the azimuthal wave number in outflow zone (for more details see Sect. 3.1)

For the PIV and PLIF measurements, a square chamber was placed outside the glass cylinder and filled with the working fluid to reduce the refraction effects caused by the curved surface of the cylinder. The working fluid was a mixture of water and potassium thiocyanate KSCN (weigh concentration 64 %, $\rho = 1,400$ kg m^{-3}, $\mu = 2.4 \times 10^{-3}$ Pa s, $n_D = 1.472$) which has the same refractive index as the outer cylinder's glass. The temperature of the working fluid (i.e., room temperature 20 °C), varied by no more than 0.5 °C over the course of the experiments. A variation of 1 °C results in a variation of <0.1 % of the refractive index n_D of KSCN solution and 1.2 % of fluorescence (Sakakibara et al. 1993) for this tracer.

2.2 Measurement techniques

The flow and mixing in the Taylor–Couette device were quantified by particle image velocimetry (PIV) and planar laser-induced fluorescence (PLIF). PIV and PLIF systems

Fig. 3 Schematic of the experimental setup, PIV and PLIF systems. Telecentric lenses were mounted on both cameras
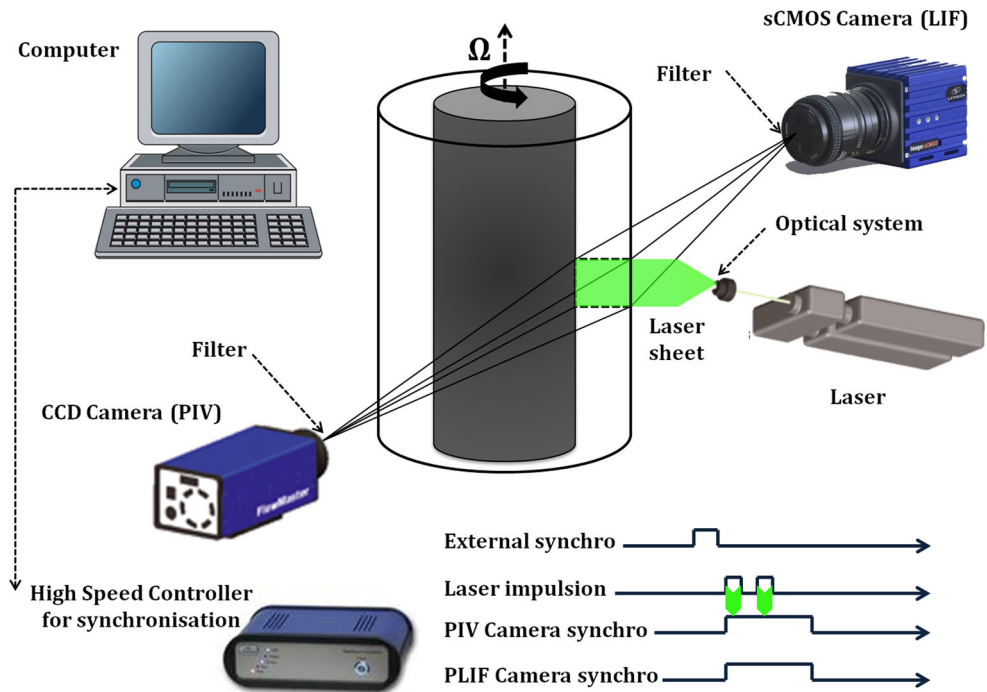
were synchronized. The experimental setup is shown schematically in Fig. 3.

A PLIF system was used to measure the concentration across the meridional plane $(r - x)$ of the gap. We used a dual ND: YAG laser $(2 \times 200$ mJ, $\lambda = 532$ nm) to illuminate the measurement plane. LIF images were recorded using an sCMOS camera with $2{,}560 \times 2{,}160$ pixels and a high-pass optical filter $(\lambda \succ 540$ nm) suited to the dye emission spectrum. A fluorescent tracer consisting of Rhodamine WT was carefully injected, over approximately 10 s, into the flow through an orifice at the center of the test rig, at the vortex A (see Figs. 9, 10). Rhodamine WT has a maximum absorption wavelength at 565 nm, a maximum emission wavelength at 585 nm and a low temperature and pH sensitivity. So it is particularly suitable for this application. A software and a timing box were used to synchronize the laser with the camera and the PIV system.

Before running the experiments, many preliminary tests were performed in order to guaranty results of high quality. For calibration, images of fully mixed dye solution of various concentrations were recorded and then a calibration curve was established. A suitable injection quantity was chosen to provide adequate dynamic resolution without exceeding the limits for linearity $(0 < C_0 < 5 \times 10^{-3}$ g $L^{-1})$. All concentration measurements are normalized by the injection concentration C_0. Then an appropriate injection rate was determined to avoid any flow perturbation. A small amount of dye was mixed with the solution in the quiescent outer chamber and imaged with the flow to verify the consistency of the laser pulse intensity. Indeed, the

laser may have pulse to pulse variations of delivered energy. This can flaw the quantitative measurement of the concentration during mixing. Therefore, this measure in the outer chamber is used to scale instantaneous measurements and enforce consistency. Moreover, no photo-bleaching has been observed. LIF measurements were recorded across a section of the meridional $(r - x)$ plane at 10 Hz for different Re. The measurement region was restricted to an axial range of $8.16 \times e$ and a radial range equal to e, in the middle of the rig. For each case, 5,000 concentration fields were recorded.

For PIV measurements, particle field images were recorded using a PCO.2000 camera with a CCD captor of $2{,}048 \times 2{,}048$ pixels and a narrow band-pass optical filter around 532 nm. A telecentric lens was mounted on the camera to avoid parallax distortion along the narrow annulus (this prevents any spurious projection of the azimuthal velocity in the radial plane of measure). The working fluid was seeded with silver-coated hollow glass spheres with density 1.4 kg m^{-3} and an average diameter of 10 μm. Those particles are neutrally buoyant in KSCN at the concentration we used for index matching. For each Reynolds number at which velocity measurements were made, the annulus was filled with fluid, and the inner cylinder was run at high speed for a few minutes to mix the fluid and the tracer particles. Then the inner cylinder speed was ramped to the desired speed using a specified start-up protocol. After the inner cylinder had reached the desired speed, the flow was allowed to develop for at least 10–15 min to ensure fully developed flow before the

measurements began. Holding the inner cylinder speed constant and repeating the measurements some time later showed that this procedure generated repeatable results. Because of the limited front lens diameter of the telecentric lens, the illuminated measurement plane was set to $5.7 \times e$ in the axial direction to make sure that at least two full vortices are captured. Typically, 500–800 image pairs were acquired at 10 Hz, corresponding to the passage of 8–18 azimuthal waves. Velocity vectors were calculated on a square grid (16×16) with sub-pixel intercorrelation.

The uncertainty on the Reynolds number due to the variation in the inner cylinder speed, fluid viscosity, and other factors was at most 5 %. The uncertainty on the velocity measurements depends on several factors (peak locking, correlation technique and interpolation scheme, density mismatch between tracer particles and fluid). We have chosen to use hollow glass particles, because density matching of those particles with our solution is very good. The other sources of error have been controlled based on PIV state of the art. As a validation test, PIV measurements of the pure azimuthal Couette flow were performed to check accuracy (in a radial plane, the velocity should be zero). The maximum of spurious velocities we measured was of the order of 1 % of the inner cylinder speed

regarding axial component; and 2 % for the radial component.

3 Velocity and concentration fields

3.1 Flow characterization

Flow fields have been measured to characterize each regime (in our case TVF and WVF flows). They provide information on the shape of the vortices and the wave state (λ_x and m). Preliminary flow patterns visualizations indicate that the transition to TVF flow occurs at a critical Reynolds number $Re_c = 80$. For this regime, instantaneous velocity fields show no significant motion of the boundaries between vortices, and negligible deformation of the shape of each vortex. The average axial wavelength is approximately $\lambda_x = 2.01 \times e$. Since the shapes of the vortex do not change and the boundaries between them are fixed (see Fig. 4), quantifying the transport within a vortex or between adjacent vortices is easier than for WVF, as shown by Dusting and Balabani (2009).

In contrast, for WVF flow, the velocity field changes significantly and the relative shape and position of each

Fig. 4 Instantaneous velocity field over one period at $Re = 382$ (TVF) and $Re = 795$ (WVF): from *top* to *bottom*: **a** $\Phi = 0$, **b** $\Phi = 0.25$, **c** $\Phi = 0.5$, **d** $\Phi = 0.75$, **e** $\Phi = 1$
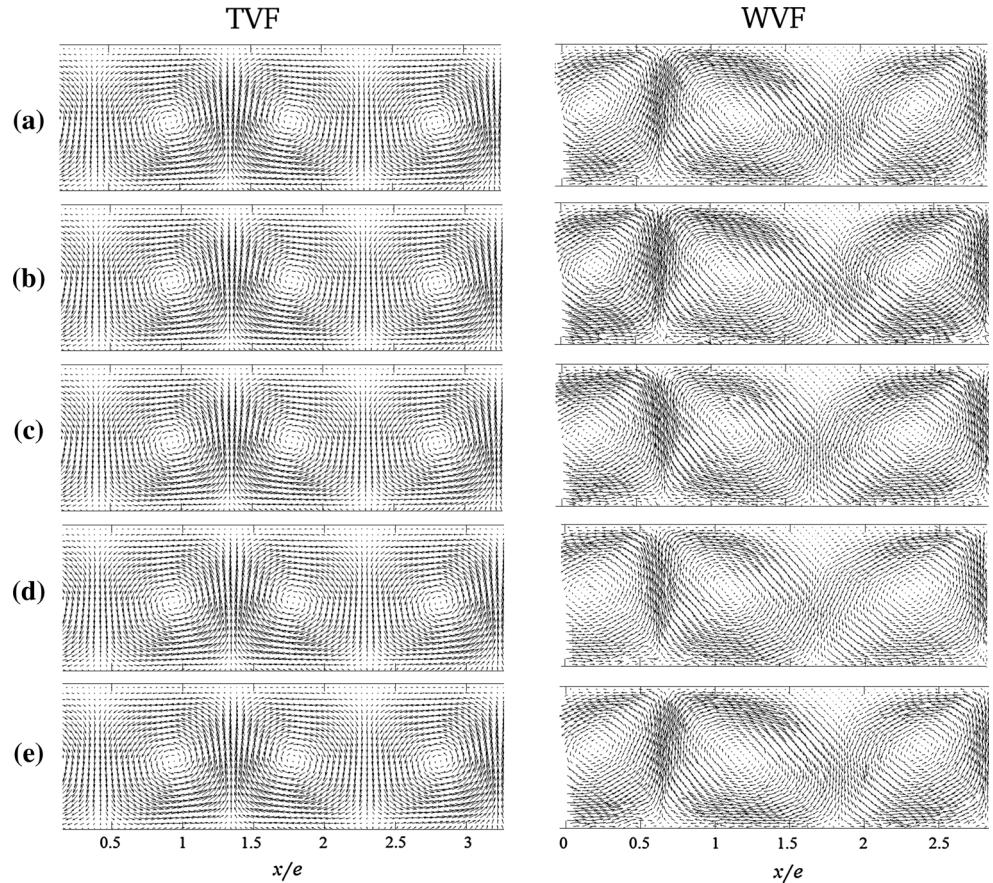
vortex also vary in time (see Fig. 4). The flow became three dimensional. It is characterized by an axial motion responsible for the deformation of vortices, and a significant dye transport in the axial direction. Wereley and Lueptow (1999) have described in details the characteristics of this flow, especially axial transport.

When the wavy vortex flow is reached, the vortices oscillate both axially and radially. During one period, the vortex volume first grows, as a significant portion of fluid from neighboring vortex is transferred due to an upward stream, and then shrinks, as the cell loses fluid to the benefit of its adjacent vortex (downward stream). Both vortex cores and separating boundaries are experiencing periodic motion.

In our configuration ($\eta = 0.687$), the wave motion appears to be more pronounced in the inflow zone than in the outflow one (inflow, respectively, outflow, stands for fluid motion toward the inner, respectively, outer cylinder). In fact, as can be seen in Fig. 5, there is a significant difference in wave motion (amplitude and wave number and frequency) between the two near-wall regions. In inflow zone, the inclination of the "jet-like" boundary could reach 45° in the two directions. Andereck et al. (1985) refer to these flows as the wavy inflow- and outflow-boundary flows (WIB and WOB, respectively). WIB and WOB are, respectively, exhibiting a flat and a wavy boundary, or, at least, wavy boundaries with different angular speed and azimuthal wavenumber m, as confirmed by our observations (Fig. 2; Table 2). Imomoh et al. (2010)
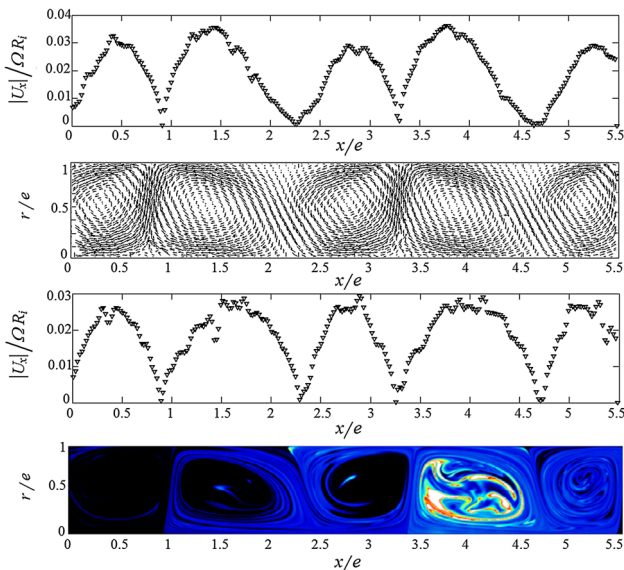

Fig. 6 Position evolution of the boundaries between adjacent vortices ($Re = 795$), (*black*) inflow zone and (*blue*) outflow zone
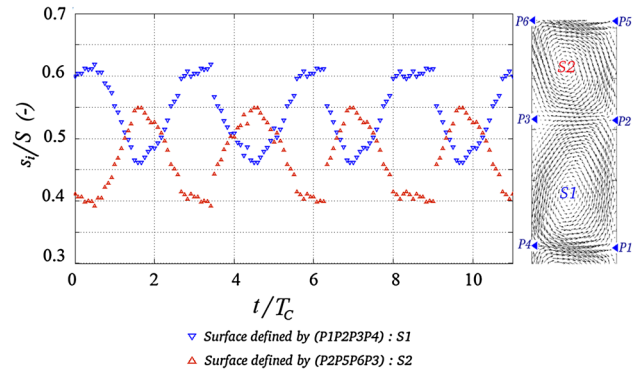
Fig. 7 Vortex size evolution of two adjacent vortices over some revolutions of the inner cylinder ($Re = 795$)

also showed that inflow and outflow boundaries have different spectral characteristics. In order to track this motion, we followed the evolution of the velocity magnitude for the axial component at $r/e = 1$ (outer wall) and $r/e = 0$ (inner cylinder). The minimum magnitude, occurring near walls, corresponds to the position of a boundary. The result of the tracking is presented in Fig. 5. The variation of the position of inflow and outflow boundaries is shown in Fig. 6 and vortex size in Fig. 7.

The results confirm that the displacement is more pronounced in inflow than in outflow zones. The magnitude can reach 5 mm (i.e., $\approx e/2$), while it is less than 0.6 mm for the outflow side. This could be explained by the magnitude of the wave in inflow zone compared to outflow zone.

To estimate the evolution of each vortex size due to the azimuthal traveling wave, we relied on the tracking method previously explained, which is based on PIV measurements (velocity profiles in Fig. 5). Indeed, at each instant, based on the positions of the limits defining each vortex, denoted P_i, we calculated the instantaneous area of each vortex, denoted $s_i(t)$. The computed area is then normalized by the area of a Taylor-cell (formed by two adjacent counter-

Fig. 5 Tracking of boundaries between adjacent vortices (WVF: $Re = 795$), from *top* to *bottom*: axial component of velocity $|U_x|$ near the outer cylinder ($r/e = 1$), instantaneous velocity vector field, axial component of velocity $|U_x|$ near the inner cylinder ($r/e = 0$) and instantaneous concentration field
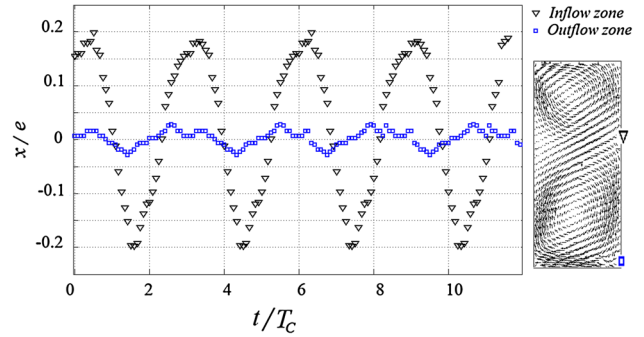
rotating vortices which correspond to an axial wavelength λ_x), denoted S. An example of results is shown in Fig. 7. The results show that the vortex size can vary between 35 and 65 % of the size of the Taylor-cell ($S \approx cte$). The degree of variation is directly related to the wave state and particularly the wave amplitude.

The positions of the boundaries between adjacent vortices, thus determined from velocity field, were used to monitor the vortex oscillation with time, in order to achieve accurate calculation of the concentration field in wavy regimes.

The non-uniqueness of flow (Coles 1965; Rudman 1998; Dutcher and Muller 2009) was also observed through the existence of hysteresis phenomena. Multiple stable flow states could be reached for a given Reynolds number. These various states were distinguished by the axial wavelength λ_x, ranging from $2.01 \times e$ to $2.5 \times e$ and the azimuthal wave number m, ranging from 2 to 8. Different wave states (λ_x, m) were produced by approaching the target Reynolds number Re with specific start-up protocols, as presented in Sect. 2.1.

3.2 Concentration field: observations

After dye injection, the time evolution of the fluorescent tracer mixing was recorded and analyzed. The tracer is injected with a capillary located close to the center of vortices (injection flow rate has been adapted to local fluid velocity to minimize flow perturbations). The period T_d of the temporal oscillation of the concentration observed in Fig. 8 is the time required for a fluid element to make a full rotation over the inner cylinder. This dyed fluid element is advected by the azimuthal component of the flow field. It is determined by following the average concentration in a small region near the center of a vortex (Fig. 8). It was
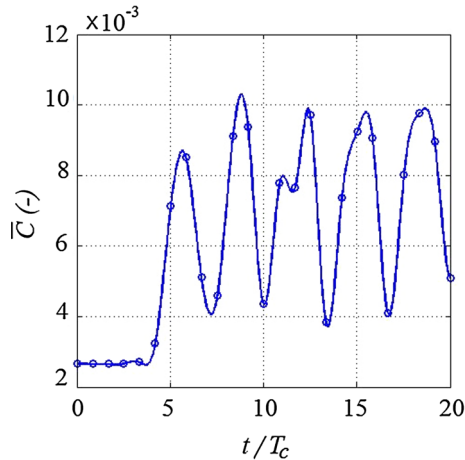

Fig. 8 Temporal evolution of the concentration near the core of vortex A, for $Re = 382$. Four periods T_d are displayed
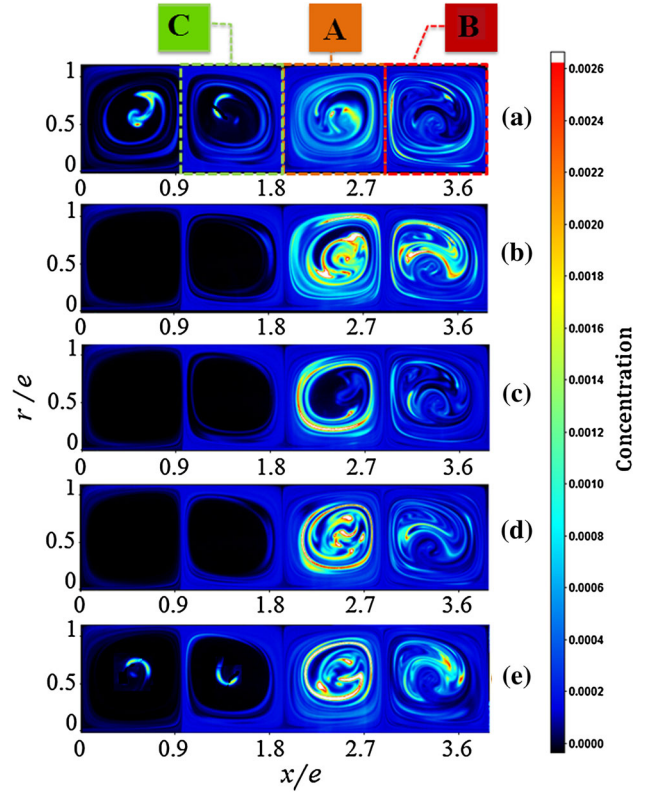

Fig. 9 Instantaneous concentration fields over one period at $Re = 382$ (TVF); from *top* to *bottom*: **a** $\Phi = 0$, **b** $\Phi = 0.25$, **c** $\Phi = 0.5$, **d** $\Phi = 0.75$, **e** $\Phi = 1$

estimated to be $T_d = 3.6 \times T_c$. The distribution of instantaneous concentration, at different phase shift Φ over one period T_d, is presented in Figs. 9 and 10 for TVF regime ($Re = 382$) and for WVF regime ($Re = 1,082$), respectively. The dye phase shift, Φ, is normalized by 2π, and the concentration is normalized by the injection concentration C_0.

For the TVF regime, observations showed the formation of an intense narrow tracer layer close to vortex interfaces, just after the injection. Tracer remains confined in outer layers before being convected toward the next interface where it can again be transported to the neighboring vortices. Although the boundaries between adjacent vortices stay straight, evidence of tracer transport between neighboring vortices was observed, more specifically in near-wall regions (Desmet et al. 1996a, b; Campero and Vigil 1997). These observations contradict the usual assumption of non-intermixing in TVF flow, made in many chemical engineering studies (Kataoka et al. 1975; Tam and Swinney 1987; Moore and Cooney 1995). On the other hand, the inner regions correspond to poorly mixed vortex cores where the mixing is low. Tracer is transported very slowly toward those zones and mixing is basically achieved by molecular diffusion. The 2-zone model, proposed by Desmet et al. (1996a), is therefore more representative of the
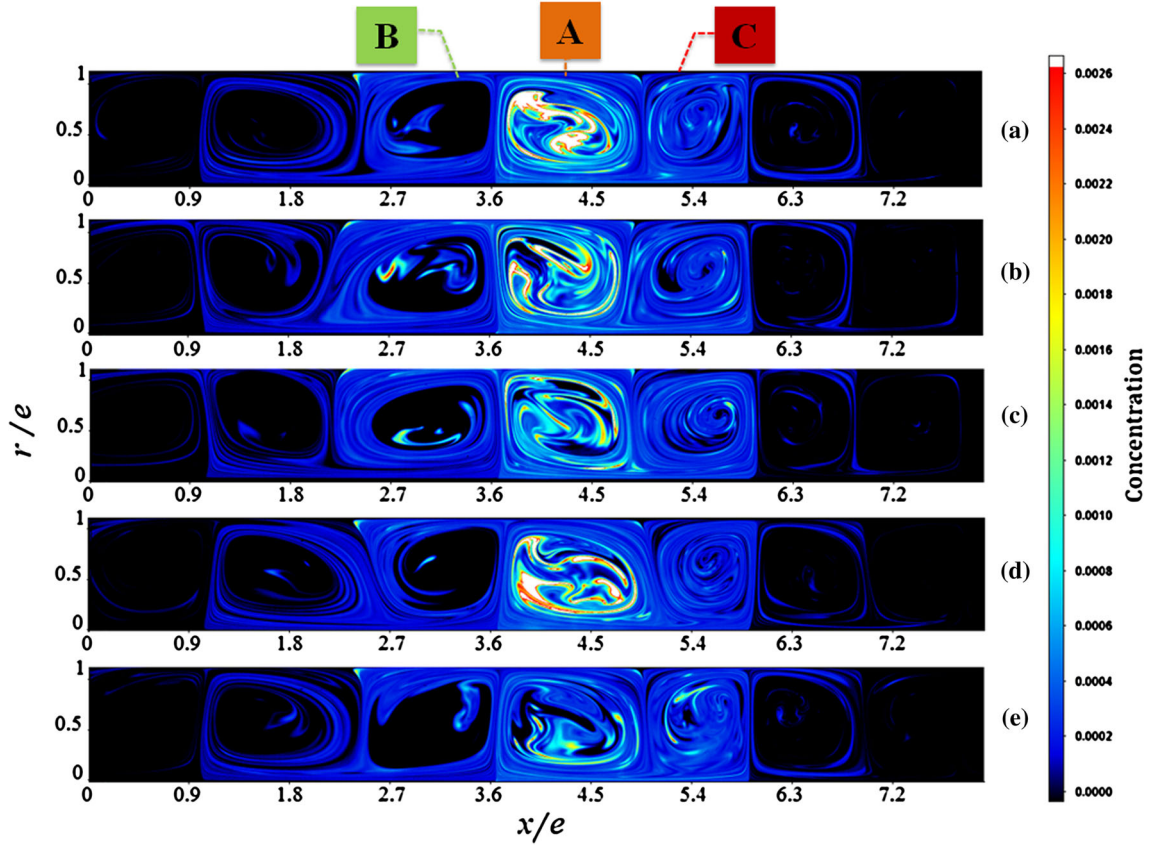
Fig. 10 Instantaneous concentration fields over one period at $Re = 1{,}082$ (WVF); from *top* to *bottom*: **a** $\Phi = 0$, **b** $\Phi = 0.25$, **c** $\Phi = 0.5$, **d** $\Phi = 0.75$, **e** $\Phi = 1$

transport in TVF regime, where the outer zone would represent the well-mixed region and the inner one would correspond to the vortex core.

As the rotation rate is increased, the TVF flow symmetry is broken and wavy regimes are emerging. The apparition of traveling wave breaks the boundaries between adjacent vortices and enhances fluid exchange. The snapshots of the concentration field presented in Fig. 10 show that tracer transport between vortices is more efficient. In fact, the velocity field became three dimensional, leading the flow to be more chaotic, increasing significantly its capacity to advect, stretch and diffuse the tracer concentration.

However, Fig. 10 exhibits also the persistence of poorly mixed vortex cores where tracer can be trapped. Their presence in WVF regime was first observed numerically by Rudman (1998) using Poincaré sections, derived from fluid particle trajectories, and visualized experimentally afterward using a bichromatic acid-base chemical reaction technique (Rudman et al. 2008). The vortex core volume was estimated to approximately 40 % of the total vortex volume by Campero and Vigil (1997) for TVF flow.

On the other hand, the estimation of the unmixed core volume in WVF regime is not straightforward, since its boundaries are evolving due to the traveling wave: Its

position and its apparent size vary over time with the passage of the azimuthal wave. Rudman (1998) has estimated the core volume by performing numerical tracking of many fluid particles. Variation between 5 and 20 %, depending on the wave state, were obtained, thus influencing axial dispersion and mixing properties. Although poorly mixed cores are still observed in WVF regime, the wave induced motion contributes strongly to their volume reduction and partially cancels their contribution. In fact, the wave pushes the fluid into the poorly mixed zones where molecular diffusion will neutralize the cores as well.

Observations also show that tracer transport at inflow boundaries is different from transport at outflow boundaries. This could be explained by the velocity field previously discussed. The deformation related to wave state (wave amplitude and wave number m) is more intense in inflow zones. The intervortex mixing in these two zones is further discussed in the following section.

4 Mixing properties

Following the work of Dusting and Balabani (2009) for the TVF regime, we have considered three adjacent vortices A,

B and C to investigate intra- and intervortex mixing in the TVF and WVF flow patterns (see Figs. 9, 10). A stands for the vortex where the dye is injected, B for the outflow-adjacent vortex to A, and C is the inflow-adjacent vortex to A. The segregation intensity parameter I was used to quantify the inter and intravortex mixing. It is defined by Eq. 2:

$$I = \frac{\sigma_c^2}{\sigma_0^2} \qquad (2)$$

with:

$$\begin{cases} \overline{C} = \dfrac{\sum C_i}{N} \\ \sigma_c^2 = \dfrac{1}{N-1}\sum(C_i - \overline{C})^2 \\ \sigma_0^2 = \overline{C}(1 - \overline{C}) \end{cases} \qquad (3)$$

where $\overline{C}$ is the average normalized concentration (concentration C_i has been scaled by C_0) formed over N time frames, σ_c the standard deviation of concentration and σ_0 the maximum mean concentration. I tends to zero when the perfectly-mixed state is reached.

In order to investigate mixing over the different directions, different definitions of the mean concentration and the variance have been considered:

- I_v characterizes the intervortex mixing between vortices A and B or A and C. C_i is the average concentration over the spatial region occupied by each vortex, while $\overline{C}$ is the average concentration over two adjacent vortices. (e.g., for vortices A and B, C_i corresponds to $i = A$ for vortex A, $i = B$ for vortex B and $\overline{C} = (C_A + C_B)/2$).
- I_{rx} characterizes the intravortex mixing in the meridional plane, by considering the average concentration over one period of the azimuthal wave (thus removing the phase dependence).
- I_θ characterizes the intravortex mixing in the azimuthal direction, by considering the average concentration over the $r - x$ plane (thus removing the spatial dependence in r and x).

Another parameter used to determine the mixing efficiency is the rate at which neighboring fluid elements are stretched apart. Following Ottino (1989), the rate of stretching is based on the deformation of a surface, from its reference area dA to its actual state, da. The area stretch, noted s, is defined by:

$$s = \frac{da}{dA} \qquad (4)$$

The rate of stretching is then defined as:
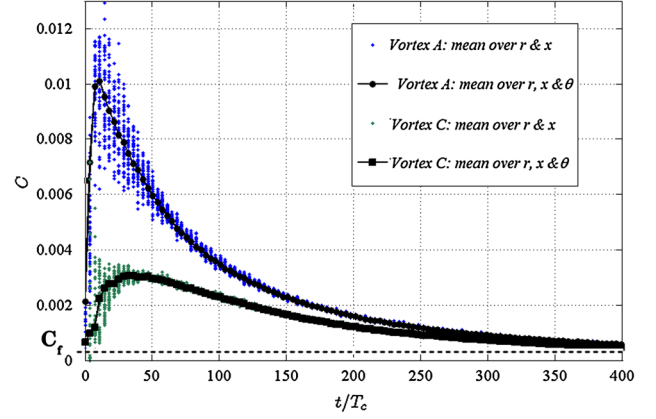
$$S_a = \frac{d\ln(s)}{dt} \qquad (5)$$

Fig. 11 Temporal evolution of the average concentration in vortex A and C ($Re = 1,082$). C is normalized by the injection concentration C_0

In order to evaluate S_a from the PLIF instantaneous concentration fields, an appropriate threshold was chosen for the image binarization. Then, the relevant surface area a was defined as the area of pixels with value 1, and its deformation and growth over time were measured.

The average concentration in each vortex is presented in Fig. 11. The small blue dots stand for the $r - x$ average concentration and depict the concentration variation over each period T_d. The larger black dots represent the average concentration over the full period. The plot shows that each vortex concentration converges to the final concentration C_f corresponding to perfect mixing. For WVF regime ($Re = 1,082$), 300 revolutions of the inner cylinder are sufficient to reach the final concentration C_f. While for TVF regime ($Re = 382$), more than 1,500 revolutions are required.

4.1 Mixing in TVF regime

4.1.1 Intravortex mixing

Mixing within a vortex results from the combination of mixing in the azimuthal direction and mixing in the meridional plane. The intensity of segregation in the azimuthal direction and across the meridional plane is plotted in Fig. 12 for the three vortices under consideration: A, B and C.

Mixing in the azimuthal direction is very efficient. The timescale of mixing in $(r - x)$ plane is approximately four times longer than in the azimuthal direction θ. This was expected, since the azimuthal component of the velocity field, and its gradient, is large compared to the $(r - x)$-plane values. Mixing in the meridional plane is very weak compared to other directions and even compared to intervortex mixing. This could be explained by the presence of
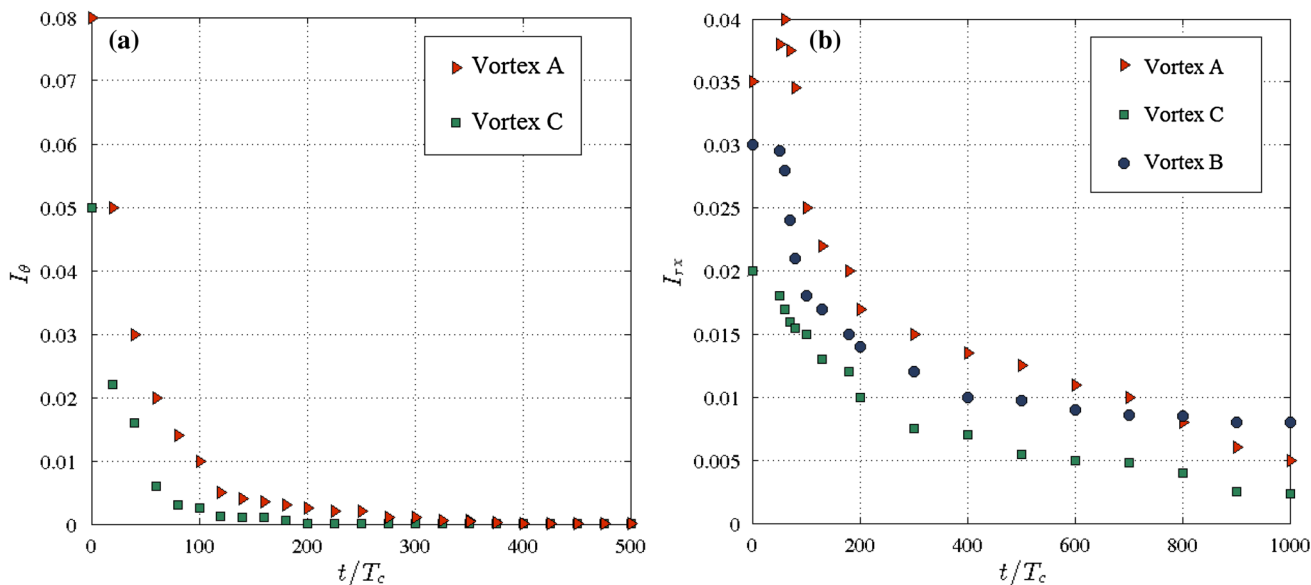
Fig. 12 Intravortex mixing ($Re = 382$): **a** Intravortex mixing in the azimuthal direction for vortex A and C, I_θ and **b** Intravortex mixing in the meridional plane for vortex A, B and C, I_{rx}

many zones in the $(r - x)$ plane where the mixing efficiency is weak, and especially the vortex core where only diffusion is effective as shown in Sect. 3.2 (Desmet et al. 1996a; Rudman et al. 2008). This explains why the mixing process in the meridional plane is not spatially uniform.

The mixing timescale in the outer zone is significantly shorter than in the vortex core. Dusting and Balabani (2009) have confirmed this feature by dividing the vortex into different subregions. Their results showed that in the vortex core, where the axial and radial components of the velocity field are nearly zero, a longer time is required to achieve uniform dye concentration. This result demonstrates again that mixing in the vortex core is driven by molecular diffusion only.

The degree of intravortex mixing can also be estimated by analyzing the temporal growth rate of the surface area a in order to estimate its rate of stretching. At each investigated Reynolds number, Re, the stretching was first calculated for every images then period-averaged to remove the phase dependence. Figure 13 shows the temporal evolution of area stretching for two flow regimes, TVF and WVF. Results highlight that stretching rate s increases exponentially with time. This indicates that neighboring tracer elements are being stretched apart by flow gradients, improving the ability of the flow to mix the tracer. The flow field can produce very efficient stretching and folding in the measurement plane. The rate of stretching increases with the Reynolds number, Re. For TVF regime, mixing is less efficient. Tracer elements are trapped into vortices especially near the vortex center. While moving along the azimuthal direction, they remain trapped in the same
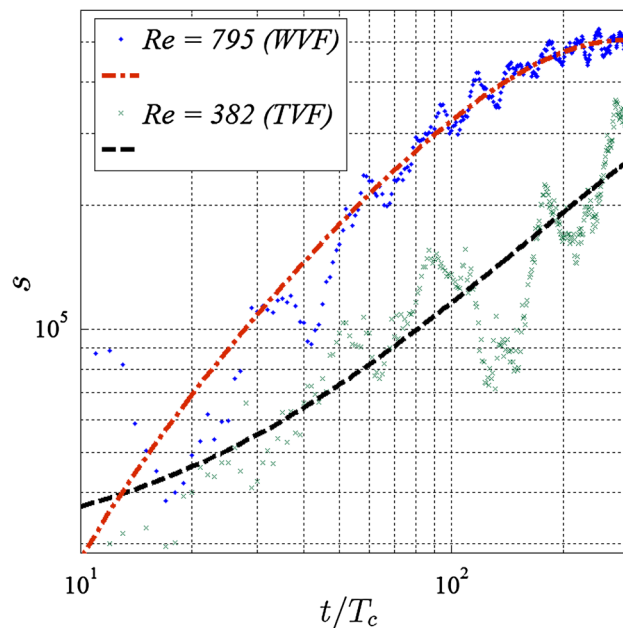

Fig. 13 Intravortex mixing: strain rate as function of time

vortex. In contrast, dye located between vortices boundaries (inflow and outflow zones) have more chances to be transported between adjacent vortices, creating then more tracer area which leads to the growth of s. On the other hand, for WVF regime, tracer has penetrated more vortices creating more area which indicates better mixing within vortices (intravortex mixing) as well as more efficient axial transport between vortices (intervortex mixing). The chaotic motion, characteristic of this regime, provides more
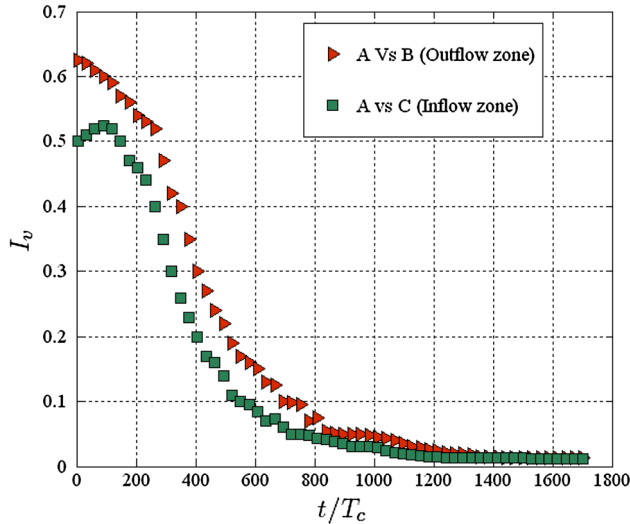
Fig. 14 Intervortex mixing I_v between vortex A and B, A and C ($Re = 382$)

stretching and folding of tracer surfaces, yielding very efficient area generation and mixing.

4.1.2 Intervortex mixing

To investigate intervortex mixing, we consider the three adjacent vortices, A, B and C. A is separated from B by an outflow zone and from C by an inflow zone. The intensity of segregation I_v between A–B and A–C is plotted in Fig. 14. The respective temporal decay characterizes the dye dispersion between the vortices. Timescale of this intercell mixing is shorter than intravortex mixing across the meridional plane. It is achieved at $t/T_c = 1,200$ while in Fig. 12b, we can observe that perfect mixing is not reached yet. A simple extrapolation shows that mixing index approaching zero will be achieved for time $t/T_c > 1,200$. Therefore, the mean concentration in neighboring vortices converges to the final concentration in a shorter time than the concentration in a single vortex. Again, this result contradicts the common assumption that mass transport in TVF flow can be modeled as series of well-mixed tanks (Kataoka et al. 1975; Tam and Swinney 1987; Moore and Cooney 1995).

Indeed, intervortex mixing in TVF regime, which is basically due to molecular diffusion, is supplemented by advection in near-wall regions where hyperbolic flows can transfer concentration to the adjacent vortex. These two mechanisms are both responsible for mass transfers across adjacent vortices, located, respectively, in regions near the inner layers and at the inflow boundaries.

Thus, in TVF flow, the slow intravortex diffusion imposes the tracer to remain in these regions before being rapidly transmitted by convection to the adjacent vortex

and so on. Finally, our results do not show noticeable differences between intermixing over the inflow and outflow cell boundaries.

4.2 Mixing in wavy regime

As previously mentioned, in TVF regime, the velocity field is axisymmetric and mixing is slow. As the Reynolds number is further increased beyond $Re = 400$, the velocity field becomes dependent on all three spatial directions and the flow symmetry is broken. This results in an enhancement of the two main mechanisms of mixing. First, the KAM tori structure is destroyed leading to chaotic advection and consequently enhanced intravortex mixing. Then, the wavy perturbation breaks the boundaries separating adjacent vortices leading to intervortex mixing.

4.2.1 Intravortex mixing

Index of segregation in the azimuthal direction I_θ and across the meridional plane I_{rx} are plotted in Figs. 15 and 18 for $Re = 795$ and $Re = 1,082$, respectively. The plots show that mixing in tangential and meridional directions increase significantly for WVF regime. Only 50 rotations of the inner cylinder are necessary to achieve homogeneity of the concentration in the azimuthal direction. Hence, the mixing timescale is significantly reduced compared to TVF regime. It is approximately 6 times ($Re = 795$) and 10 times ($Re = 1,082$) shorter than at $Re = 382$ (the time is normalized by the inner cylinder rotation period). This is directly linked to the velocity field characteristics that increase the vortex capacity to stretch and advect passive tracers.

The appearance of the waviness also causes the "disintegration" of KAM tori, resulting in an increase of the degree of vortex distortion. The wave is able to convect fluid deeper into the unmixed vortex cores, thus decreasing the volume of the unmixed core and increasing the volume of the well-mixed outer layers. This results in an enhanced intravortex mixing. The respective mixing efficiency in azimuthal and meridional plane is reduced, compared to TVF regime. However, unlike Dusting and Balabani (2009), we found that mixing over the azimuthal direction remains more important due to the high azimuthal velocity and its gradients. This could be also related to the existence of the unmixed cores, which weakens the mixing across the meridional plane, as experimentally evidenced in Sect. 3.2 and numerically observed by Rudman et al. (2008).

4.2.2 Intervortex mixing

The waviness of WVF regimes breaks the stream surfaces between neighboring vortices, which increases fluid fluxes across them. The waves indeed increase the rate of fluid
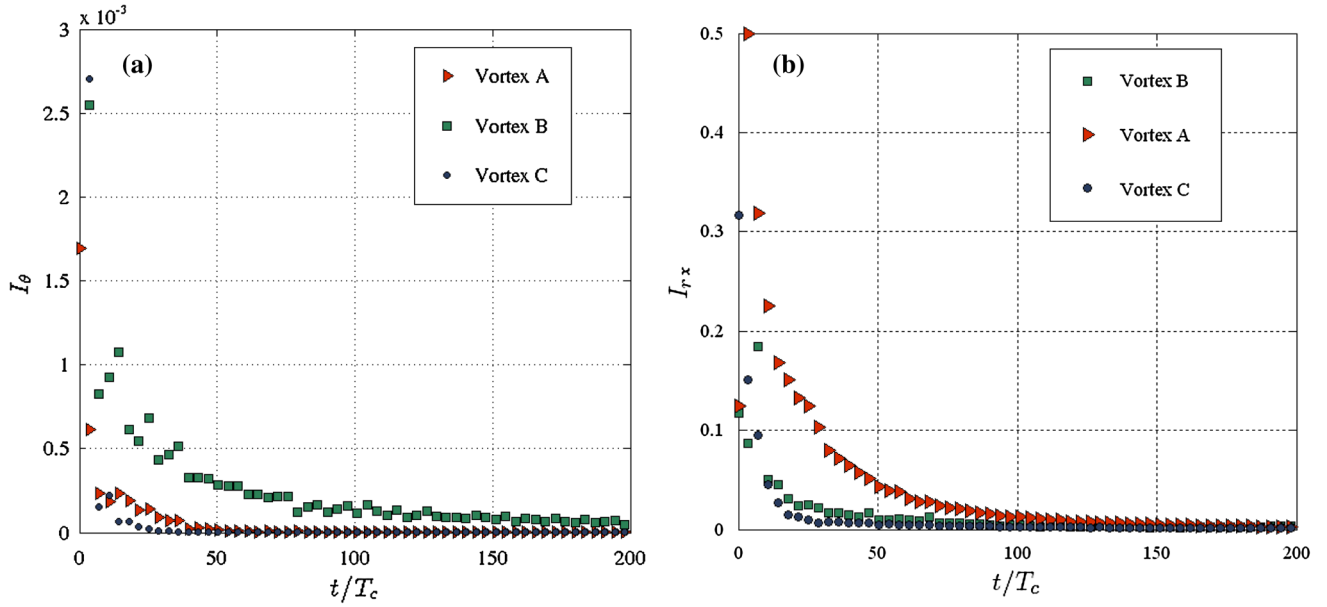
Fig. 15 Intravortex mixing for vortex A, B and C ($Re = 795$): **a** intravortex mixing I_θ in the azimuthal direction and **b** intravortex mixing I_{rx} in the meridional plane C

exchange between the outer layers of adjacent vortices. The vortex shape modifications observed during the cycle are due to the significant portion of fluid transferred from one vortex to another. Desmet et al. (1996a, b) have estimated this amount to be equal to 50 %. This results of course in a decrease of the intercell mixing timescale. The latter appeared to be approximately 2 to 3 times higher than the intravortex mixing time and 10 to 20 times shorter than intervortex mixing under TVF regime. The intercell mixing timescale is depending on the Reynolds number and the wave state. It should be noted, as shown in Fig. 16 (decay of the intensity of segregation I_v), that the intercell mixing timescale is a decreasing function of the Re number.

However, a significant difference is prevailing between transport in inflow and outflow regions. Figure 16 indicates that intervortex mixing is more intense in inflow zones than in outflow zones if the wave state in the two regions is different ($Re = 795$). This could be explained by velocity field characteristics in these two zones, as discussed in Sect. 3.1 and detailed by Akonur and Lueptow (2002). The wave amplitude is more intense at the inflow surfaces compared to the outflow surfaces.

The significant enhancement of mass transport between vortices results in an increase of axial dispersion. Moreover, when the wave perturbation in the outflow zone reaches the level of the inflow zone, the intervortex mixing difference between the outflow and inflow boundaries vanishes (case at $Re = 1,082$, Fig. 16). A non-monotonic behavior was also observed regarding the wave state, which is discussed in the next section.
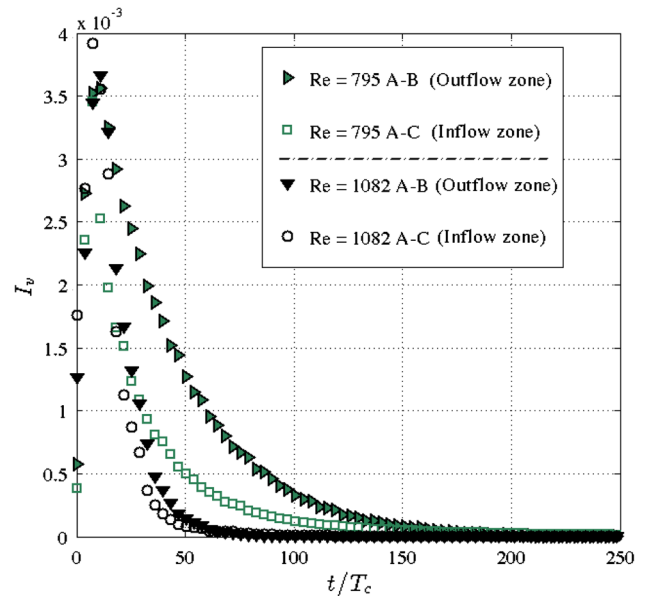

Fig. 16 Intervortex mixing between vortex A and B, A and C I_v ($Re = 795$ and $Re = 1,082$)

4.2.3 Effect of the wave state

In order to study the effect of the wave state on intra- and intervortex mixing, various wave states were considered, for two Reynolds numbers: $Re = 795$ and $Re = 1,082$. These particular flow regimes were achieved using various acceleration protocols, as detailed in Sect. 2.1. The characteristics of the different wave states are summarized in Table 2.
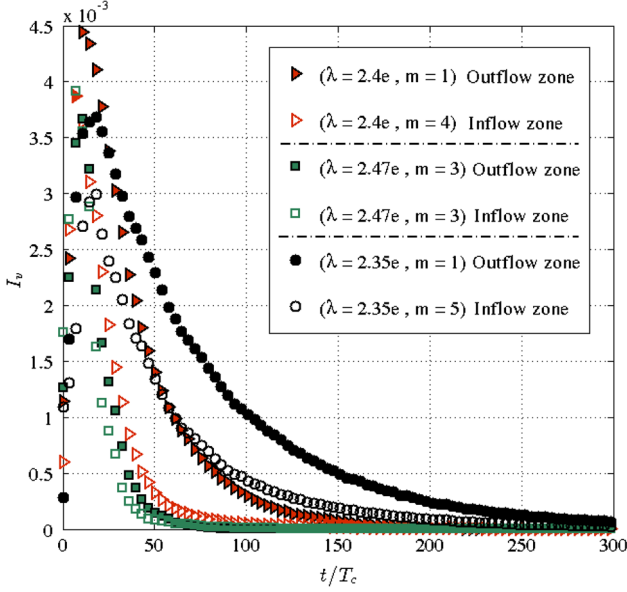
Fig. 17 Intervortex mixing between vortex A–C (inflow zone) and A–B (outflow zone), influence of the wave state ($Re = 1,082$)

Previous studies Rudman (1998), Nemri et al. (2012) showed that the property of non-uniqueness of Taylor–Couette flow could significantly influence axial dispersion. In our previous work Nemri et al. (2012), we showed that we can reach a factor 2, in terms of dispersion coefficient, for the same Reynolds number and various wave states. Rudman (1998) had also reported a factor 1.4. This non-monotonic behavior is directly related to the mixing properties, which are different depending on the flow states.

The results we obtained are plotted in terms of the intensity of the segregation, I_v, I_{rx} and I_θ for $Re = 1,082$ and three different wave states. I_v illustrates the intervortex exchange between A and B and between A and C (Fig. 17), while I_{rx} and I_θ correspond to intravortex mixing (Fig. 18).

The plots show that intervortex mixing is significantly influenced by the wave state (the axial wavelength λ_x and the wave amplitude and number m). We can note that the mixing timescale decreases with λ_x. For instance, for $\lambda_x = 2.35 \times e$, the timescale over the outflow boundaries is estimated to be twice the one corresponding to $\lambda_x = 2.4 \times e$ and three times larger than for $\lambda_x = 2.47 \times e$. Indeed, longer axial wavelength leads to greater distance traveled by the fluid in each vortex.

In the outflow zone, the mass transport appears to be enhanced in the configurations where the amplitude of the traveling wave is large. When the inflow boundaries are modulated by the wavy perturbation ($\lambda_x = 2.47 \times e$), the rate of mass transfer increases dramatically compared to cases of weakly rippling inflow zones ($\lambda_x = 2.35 \times e$ and $\lambda_x = 2.4 \times e$). In the case $\lambda_x = 2.47 \times e$, the wave number

and amplitude were the same, thus resulting in an enhanced exchange between neighboring vortices and consequently an enhanced axial dispersion. On the other hand, our results do not reveal a specific tendency of the effect of the azimuthal wavenumber m.

Finally, the results did not show obvious influence of intravortex mixing across the meridional plane and over the azimuthal direction. As can be seen in Fig. 18, the maximum difference among different cases did not exceed 5 %, in terms of intravortex mixing (I_θ and I_{rx}). Hence, the degree of intravortex mixing increases with Re, over the range we have studied, regardless of the wave state. Actually, intravortex mixing is mainly controlled by the velocity field and its gradients which increase the vortex capability to stretch and transport the dye. This could explain why for higher Reynolds the wave state effect is minor. This result is in agreement with the study of Ohmura et al. (1997a, b), who observed a weak influence of the wave state on intravortex mixing. As evidenced by our observations, they also showed that back mixing depends on the axial wavelength λ_x.

In summary, the weak effect of wave state on intravortex mixing could be explained by the nature of the velocity field in WVF regime, which counter balances or at least reduces the influence of other phenomena. Although it was not evidenced experimentally, the wave state effect on intravortex mixing was highlighted by the numerical studies performed by Rudman (1998) and more recently by King et al. (2001). This effect was attributed to the existence of non-mixing cores, which volume depends on wave state and consequently could influence axial dispersion (Rudman et al. 2008).

5 Conclusion

In this work, we focused on the dynamics of Wavy Vortex Flow in Taylor–Couette geometry and its relation with axial mixing. Thanks to simultaneous PIV–PLIF measurements, the influence of the successive flow bifurcations and wave states on intravortex and intervortex mixing was investigated experimentally. Based on PIV measurements, velocity fields have been used to characterize the flow patterns in each regime and to record the vortex temporal oscillations in order to achieve an accurate calculation of the concentration fields, especially in wavy regimes. Unlike TVF regime, for WVF regime, the relative shape and position of each vortex vary in time causing the deformation of vortices. The vortices and the jetlike boundaries oscillate both axially and radially. The mixing properties were quantified using the intensity of segregation over the different directions and between adjacent vortices.
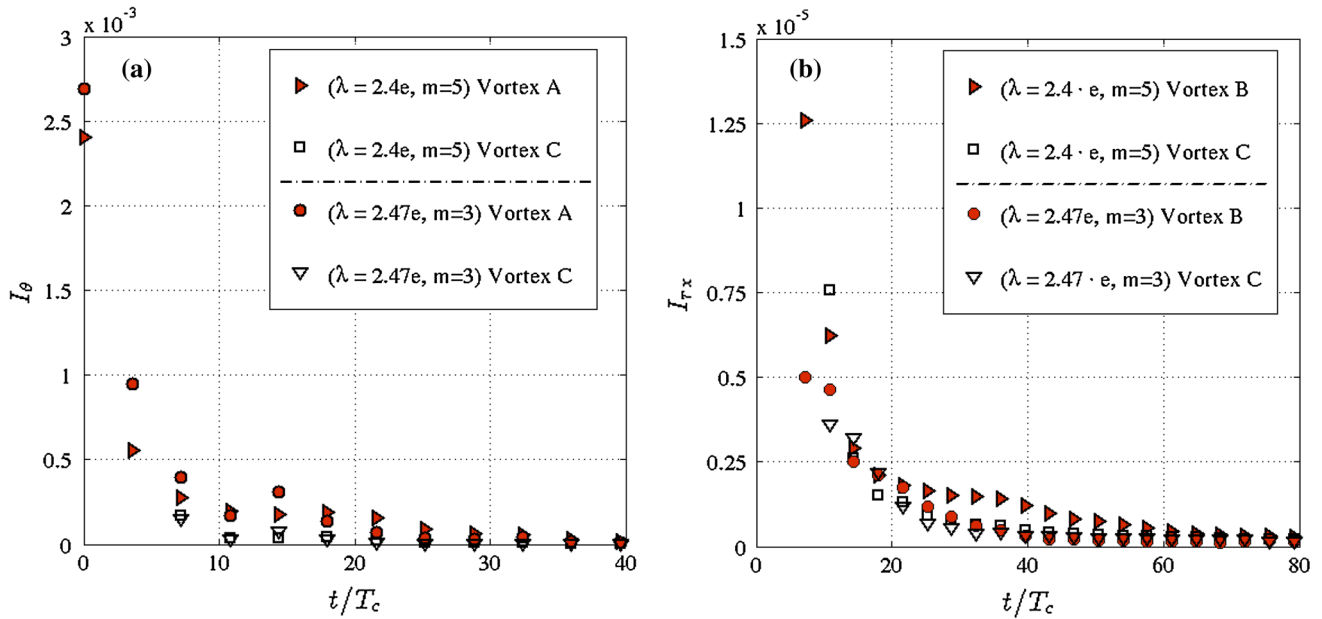
Fig. 18 Wave state effect on intravortex mixing at $Re = 1,082$. **a** Intravortex mixing in the azimuthal direction, **b** intravortex mixing in the meridional plane

PLIF results have confirmed the occurrence of intervortex mixing in TVF regime, especially in near-wall regions and across outflow boundaries. The commonly used "well-mixed stirred tanks in serie" assumption is therefore invalid for the modeling of Taylor–Couette reactors. A 2-zones model appeared to be more representative of the transport phenomena in TVF regime.

When the WVF regime emerges, the appearance of the waviness breaks the cell boundaries, which increases drastically the rate of exchange between the outer layers of neighboring vortices. This additional mode of transport enhances the axial dispersion. Since the particular velocity field prevailing in wavy regimes enhances greatly the vortex capacity to stretch and advect passive tracers, the intravortex mixing timescale is significantly reduced compared to the TVF regime. However, the persistence of unmixed cores in WVF regime limits the level of mixing across the meridional plane.

On the other hand, the decay of the intensity of segregation I_v highlighted that the transition to wavy regimes increases significantly intervortex mixing, although it remains weaker than intravortex mixing. It was also observed that intervortex mixing across inflow boundaries is often more efficient than outflow boundaries. Intercell mixing timescale decreases with the Re number.

Finally, we have also reported a non-monotonic behavior of the mixing properties with the wave state. The data illustrated that intervortex mixing is influenced significantly by the wave state, and particularly the axial wavelength λ_x and the wave amplitude. However, the results did not reveal a significant effect of the state multiplicity on intravortex mixing. The latter appeared to increase with the Reynolds number Re, regardless of the flow state.

References

Akonur A, Lueptow R (2002) Chaotic mixing and transport in wavy Taylor–Couette flow. Phys D 167:183–196

Andereck D, Liu SS, Swinney HL (1985) Flow regimes in a circular Couette system with independently rotating cylinders. J Fluid Mech 164:155–183

Campero RJ, Vigil RD (1997) Axial dispersion during low Reynolds number Taylor–Couette flow: intra vortex mixing effect. Chem Eng J 52:3305–3310

Coles D (1965) Transitions in circular Couette flow. J Fluid Mech 21:385–425

Davis MW, Weber EJ (1960) Liquid–liquid extraction between rotating concentric cylinders. Ind Eng Chem 52(11):929–934

Desmet G, Verelst H, Baron GV (1996) Local and global dispersion effect in Couette–Taylor flow—i. Description and modeling of the dispersion effects. Chem Eng J 51:1287–1298

Desmet G, Verelst H, Baron GV (1996b) Local and global dispersion effect in Couette–Taylor flow—ii. Quantative measurements and discussion of the reactor performance. Chem Eng J 51:1299–1309

Dusting J, Balabani S (2009) Mixing in Taylor–Couette reactor in the non wavy flow regime. Chem Eng Sci 64:3103–3111

Dutcher CS, Muller SJ (2009) Spatio-temporel mode dynamics and higher order transitions in high aspect ratio Newtonian Taylor–Couette flow. J Fluid Mech 641:85–113

Fenstermacher PR, Swinney HL, Gollub JP (1979) Dynamical instabilities and the transition to chaotic Taylor vortex flow. J Fluid Mech 94:103–127

Haut B, Amor HB, Coulon L, Jacquet A, Halloin V (2003) Hydrodynamics and mass transfer in a Couette–Taylor bioreactor for the culture of animal cells. Chem Eng J 58:777–784

Hill E, Krebs B, Goodall D, Howlett G, Dunstan D (2006) Shear flow induces amyloid fibril formation. Biomacromolecules 7:10–13

Imomoh E, Dusting J, Balabani S (2010) On the quasiperiodic state in a moderate aspect ratio Taylor–Couette flow. Phys Fluids 22:044103

Kataoka K, Hongo T, Fugatawa M (1975) Ideal plug-flow properties of Taylor-vortex flow. J Chem Eng Japan 8:472–476

Kataoka K, Doi H, Komai T (1977) Heat and mass transfer in Taylor-vortex flow with constant axial flow rate. Int J Heat Mass Transf 57:472–476

Kataoka K, Takigawa T (1981) Intermixing over cell boundary between Taylor vortices. AIChE J 27:504–508

Kataoka K, Ohmura N, Kouzu M, Simamura Y, Okubu M (1995) Emulsion polymerization of styrene in a continuous Taylor vortex flow reactor. Chem Eng Sci 50:1409–1416

King GP, Rowlands G, Rudman M, Yannacopoulos AN (2001) Predicting chaotic dispersion with Eulerian measures: wavy Taylor vortex flow. Phys Fluids 13:2522

Legrand J, Coeuret F (1986) Circumferential mixing in one phase and two-phase Taylor vortex flow. Chem Eng J 41:47–53

Moore C, Cooney C (1995) Axial dispersion in Taylor–Couette flow. AIChE J 41:723–727

Nemri M, Charton S, Climent E, Lanoe JY (2012) Experimental and numerical investigation on mixing and axial dispersion in Taylor–Couette flow patterns. Chem Eng Res Des 91:2346–2354

Ohmura N, Kataoka K, Shibata Y, Makino T (1997a) Effective mass diffusion over cell boundaries in Taylor–Couette flow system. Chem Eng J 52(11):1757–1765

Ohmura N, Makino T, Motomura A, Shibata Y, Kataoka K, Makino T (1997b) Intercellular mass transfer in waving/turbulent Taylor vortex flow. Int J Heat Fluid Flow 19:159–166

Ottino JM (1989) The kinematics of mixing: stretching, chaos and transport. The Press Syndicate of the University of Cambridge, Cambridge

Pudijioni PI, Tavare NS, Garside J, Nigam KDP (1992) Residence time distribution from a continuous Couette flow device. Chem Eng J 48:101–110

Rudman M (1998) Mixing and particle dispersion in the wavy vortex regime of Taylor–Couette flow. AIChE J 44(5):1015–1026

Rudman M, Metcalfe G, Lachlan J, Graham W (2008) Nonmixing vortex cores in wavy Taylor vortex flow. Phys Fluids 20:063602

Sakakibara J, Hishida K, Maeda M (1993) Measurements of thermally stratified pipe flow using image-processing techniques. Exp Fluids 16:82–96

Tam WY, Swinney HL (1987) Mass transport in turbulent Taylor–Couette flow. Phys Rev A 36:1374–1381

Taylor GI (1923) Stability of a viscous liquid contained between two rotating cylinders. Philos Trans R Soc Lond 223:289–343

Wereley ST, Lueptow RM (1999) Velocity field for Taylor–Couette flow with an axial flow. Phys Fluids 11(12):3637–3649